Chapter 6: Modeling and Bone Indentation

In this chapter, the experimental indentation testing will be combined with the finite element modeling to examine indentation modulus variability. First, scaling laws for indentation of composites will be examined. Having established that the length-scales are comparable and the phenomenon is worth investigating, a finite element model for the indentation test on a composite is developed. Finally, experimental data for indentation modulus is examined using data sets provided by a colleague, in which the local mineral density value is measured for each indentation test. These data are examined within the context of the composite modeling results in this chapter and the previous chapter, to allow for estimation of the contributions of different factors to indentation variability in mineralized tissues.

6.1 Scaling Laws for Indentation of Particulate Composites

The geometry of the particle-reinforced composite material is considered within the context of a nanoindentation experiment, in which small volumes of material are tested for their mechanical response. The hypothesis is that the nanoindentation test occurs at small enough physical length scales to sample individual features of a nanometer-scale composite ultrastructure.

One way to physically consider volume fraction is that it represents the ratio of the volume of a particle to the volume of a small element containing only that one particle (Figure 6-1), with the characteristic length of that small element (*b*) representing the interparticle spacing.

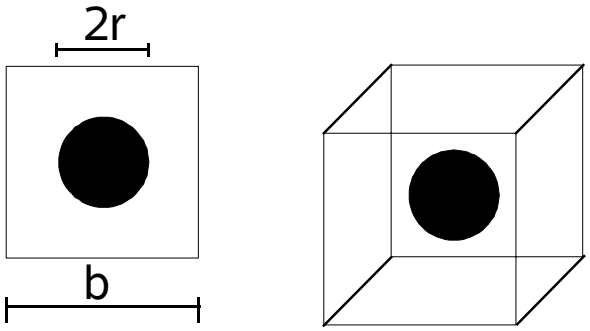

Figure 6-1: 2D and 3D unit cells for a single circular or spherical particle.

For a circular or spherical particle, radius *r*, in a square (2D) or cube (3D) with a side *b* defined as the interparticle spacing, the area fraction of particles in 2D is

$$A_F = \frac{\pi r^2}{b^2} = \pi (r/b)^2 \qquad [6\text{-}1]$$

or the volume fraction of particles in 3D is

$$V_F = \frac{4/3\pi r^3}{b^3} = 4/3\pi (r/b)^3 \qquad [6\text{-}2]$$

For a filler phase shaped as rectangular plates with width (w), length (l) and height (θ) the volume fraction of particles is:

$$V_F = \frac{wl\theta}{b^3} \qquad [6\text{-}3]$$

For rectangular particles, an effective radius r_{eff} can be defined to keep all scaling in terms of a single dimension, r:

$$r_{eff} = \left(\frac{wl\theta}{4/3\pi} \right)^{(1/3)} \qquad [6\text{-}4]$$

For bone the mineral particles vary in size but some extreme values can be examined [Currey, 2002]. For mineral particles 100 nm long, 35 nm wide and 5 nm thick, the effective radius is about 16 nm while for particles 50 nm long, 20 nm wide and 2 nm thick the effective radius is about 8 nm.

During a Berkovich indentation test, we can calculate the volume displaced by the indenter (using the approximation of a perfect conical tip, $A(h_c) = 24.5\ h_c^2$ and with no consideration for elastic displacement outside the region of contact, e.g. $h = h_c$):

$$\Delta = A\frac{h}{3} = \frac{24.5h^3}{3} \qquad [6\text{-}5]$$

The number of mineral particles encountered by the indenter is the ratio of the volume displaced by the indenter to the volume per unit cell:

$$N_P = \frac{\Delta}{b^3} = \frac{24.5h^3}{3b^3} \qquad [6\text{-}6]$$

where the volume per unit cell is directly related to the volume fraction of particles by Eqn. 6-2. For a known indenter displacement (h), a plot can be generated using Eqn. 6-6 to examine the number of particles that are "encountered" by the indenter tip for particles of different effective radii (r_{EFF}), as shown in Figure 6-2.

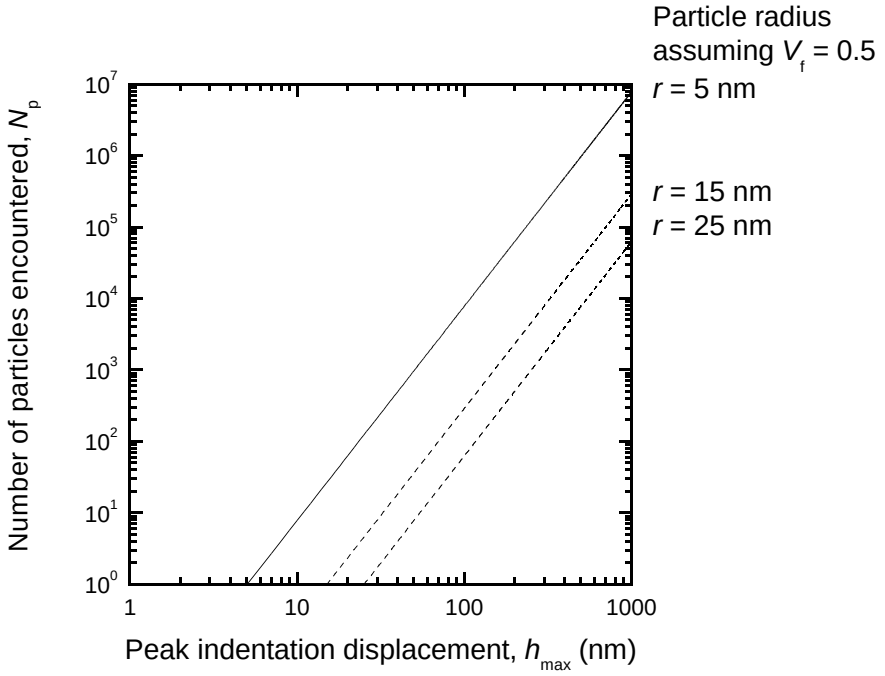

Figure 6-2: Calculated number of spherical particles (N_P) displaced by a Berkovich indenter as a function of peak indenter displacement (h_{max}).

From Figure 6-2, indentation tests performed at small but measurable peak depths (tens of nanometers) results in the indenter encountering single particles or a few particles at a time for bone mineral particles with effective radii of 5-15 nm. A degree of variability in response is therefore expected due to individual particle-indenter tip interactions in a small-load or -depth nanoindentation test on a material with nm-scale features. Small-depth tests would not be expected to present a homogeneous indentation response in materials with such nano-scale features, confirming the experimental observations seen in the experimental work presented in Section 3-3.

6.2 FEA Model for Inhomogeneous Indentation

A plane strain finite element model was constructed to examine the interaction of a Berkovich indenter tip with individual particles in a two-phase composite. A key goal of the modeling was to examine the transition from discrete particle interactions at small loads and depths to a homogenized response at large loads and depths (when the response approaches some continuum limit).

6.2.1 Model Validation for Indentation Loading

The finite element (FE) model was constructed in 2D plane strain using FlexPDE (PDE Solutions, Antioch, CA) to represent a two-dimensional block of material being indented. A rigid flat-punch was used to approximate Berkovich tip indentation. This simplification has previously been used with success for complicated material systems (*e.g.* layered systems) in which the analytic focus is on the material system and not the fundamental details of the indentation profile [King, 1987; Saha and Nix, 2002]. The approximation is justified by the obtuse angle of the Berkovich pyramid, which results in substantially larger displacements in the indentation direction compared to the lateral direction (lateral displacements are not considered in standard elastic analyses for obtuse pyramidal and conical probes).

The contact width (2D) or area (3D) is fixed in flat-punch indentation, while in Berkovich indentation the contact area increases quadratically with depth. To simulate this effect in modeling Berkovich indentation as a flat-punch, the flat punch width was increased for each indentation depth, with the width fixed to 5.6 times the displacement depth to correspond to the width to depth ratio for a Berkovich probe. The result is a contact width equivalence for the Berkovich and flat punch at each depth, as is demonstrated schematically for two different indenter depths in Figure 6-3.

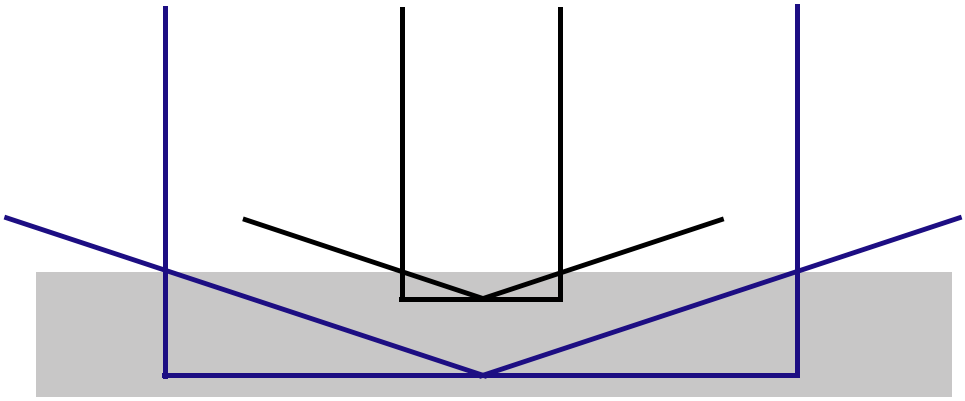

Figure 6-3: Illustration of the contact width equivalence for Berkovich and flat punch indentation when punch width is increased with indentation depth at a fixed aspect ratio characteristic of the Berkovich tip shape.

Flat punch indentation was modeled by applying a fixed *y*-displacement over a limited region of the top surface of the model. The right and left boundaries were constrained to no deformation in the *x*-direction but free in the *y*-direction (Figure 6-4).

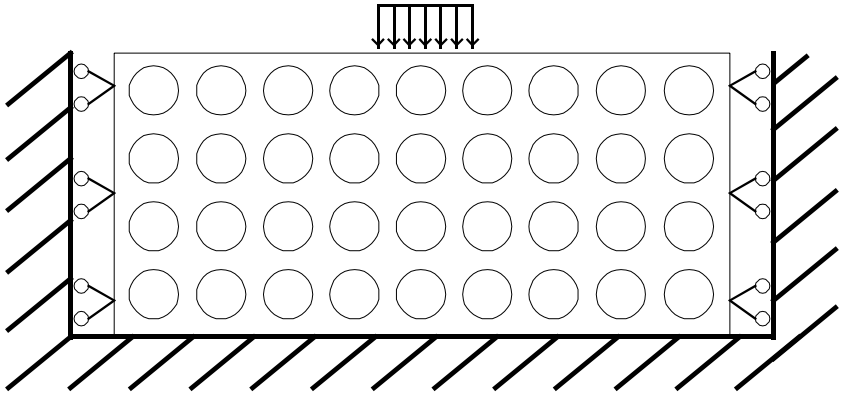

Figure 6-4: Schematic illustration of indentation model boundary conditions A fixed downward (*y*-direction) displacement was applied to the model top surface in the "indented" region.

Validation of the FEA model for flat punch indentation of a homogeneous material was considered prior to proceeding with the composite indentation model. There is no closed-form analytic solution for the plane-strain flat punch indentation problem in 2D, but the pressure distribution under the punch is known and has a simple

analytic form [Johnson, 1985]:

$$p(x)=\frac{P}{\pi\left(a^2-x^2\right)^{1/2}} \qquad [6\text{-}7]$$

where a is the contact half-width.

The surface y-stress (σ_y) profile from FEA modeling was exported as an image output and digitized. The digitized points are shown as the solid points in Figure 6-5. The center point ($x = 0$) was used to identify a value of total load P from Eqn 6-7 $\left[P=\pi a\, p(0)\right]$. The profile was plotted (solid line, Figure 6-5) and compared with the digitized FEA output (discrete points in Fig. 6-5). The two stress profiles were found to agree very well in shape, indicating at least partial validation of the FEA approach for this loading condition.

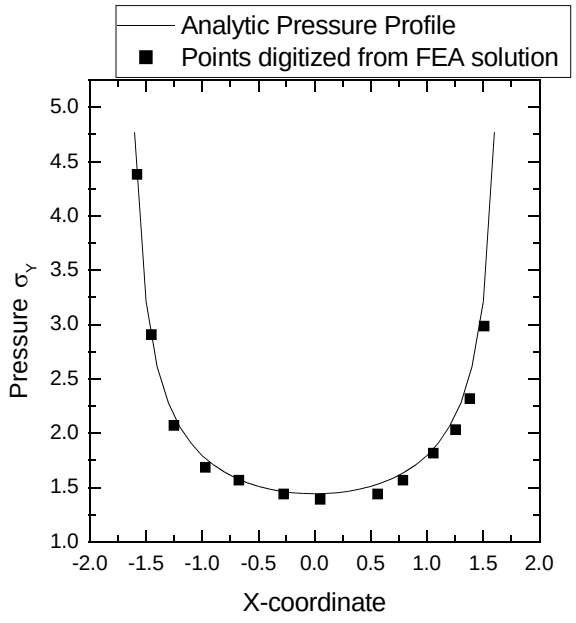

Figure 6-5: Pressure profile from flat punch indentation FE model of a homogeneous solid (discrete points) shows good agreement with the known analytical solution (solid line, from Eqn. 6-7)

6.2.2 Model for Indentation Loading of a Composite

Next the composite indentation model was examined. The finite element (FE) model was constructed in 2D plane strain using FlexPDE (PDE Solutions, Antioch, CA) to represent a two-phase composite with circular inclusions in the plane, where the circle radius (*r*) was 30 nm. The "particles" were circles and were arranged in a square array with interparticle spacing (*b*) a fixed multiple of the particle radius to vary the area fraction (and in turn the plane strain volume fraction) for each phase, as shown in Table 5-3. The model incorporated 200 particles, in 10 rows of 20 columns and was the same base model as was used for homogeneous loading in chapter 5. The key difference from the homogeneous loading model was a slightly smaller exterior "buffer" region of matrix material (*r*/10 for indentation models) from the edges of the boundary to the nearest particles, to allow displacement perturbation application to a continuous boundary but nearly directly on the particles themselves. The elastic modulus of the compliant (gelatin/collagen) phase was assumed to be 100 MPa and that of the stiff (hydroxyapatite) phase was set to 100 GPa. Poisson's ratio was assumed to be 0.3 for both phases. Models were constructed with both the stiff (apatite) and compliant (gelatin) phases as the continuous (non-particle) phase.

To examine the effect of particle volume fraction (V_F) on indentation response at large indentation depths, and to compare the indentation model to the tensile loading model results (Figure 5-4), indentation FE simulations were run for a series of different particle spacings with a fixed large displacement perturbation equal to the particle spacing (*b*) (and thus a loaded contact width of 5.6 times *b*). The nonuniform y-stress profile was integrated over the contact width to obtain the line load (P_L) for both the composite and the corresponding homogeneous loading scenario. Effective elastic modulus was calculated for the composite materials using a similar scaling as above in chapter 5 (Eqn 5-2). Indentation results were similar to the tensile results for compliant phase continuity (Figure 6-6). In the case of stiff phase continuity, effective moduli were

slightly lower than the tensile values and thus slightly below the Hashin-Shtrikman upper bound. This difference between the two loading conditions in stiff phase continuous models was greater with decreasing stiff phase volume fraction but was a relatively small effect overall. This may have been due to stress concentrations at the sharp corners of the flat punch "indenter".

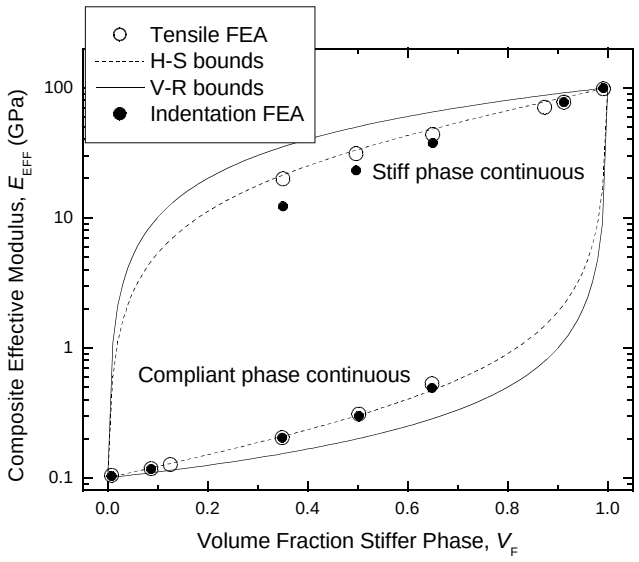

Figure 6-6: Comparison of elastic modulus (*E*) from tensile and indentation finite element results for different volume fractions (V_f) of the stiff phase.

Next, to focus on indenter interactions with individual particles at small indentation depths, indentation tests were simulated for a wide range of indentation depths (and thus contact widths) for materials with fixed volume fractions of 50% for each phase, and both stiff- and compliant- phases as the continuous phase. The center-point of load application was shifted from the continuous ("matrix") phase to the discontinuous ("particle") phase to examine local variability of responses in small-depth indentation (Figure 6-7).

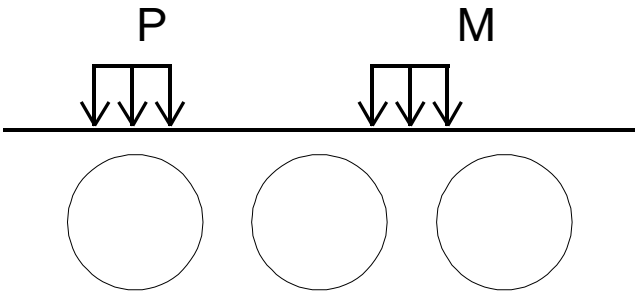

Figure 6-7: Centering of flat punch "indent" over particle (P) or matrix (M)

The flat-punch composite finite element model with contact dimension scaled to indent depth agreed with experimental Berkovich indentation response shapes, generating smooth concave-up load-displacement responses in monolithic materials (Figure 6-8). Non-smooth responses were seen for small indentation loads for composite models, reflecting the material inhomogeneity and consistent with the experimental results seen for small indentation depths (Appendix A, Figure A-2).

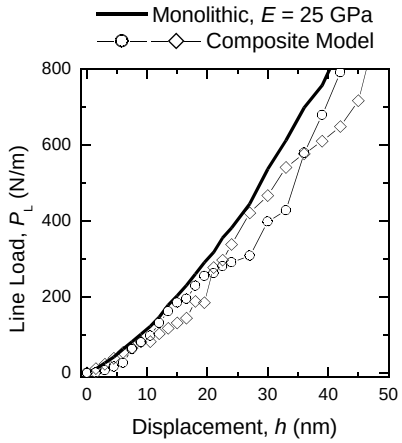

Figure 6-8: Line load-displacement (P_L-h) responses from FEA flat punch indentation. The two different composite model responses are for indent centering on particle or matrix phases.

There was also substantial variety in the calculated effective elastic modulus depending on the centering of the "punch" on "particle" or "matrix" phases at small

displacements (Figure 6-9). The modulus values for each indent centering converged to approximately the same continuum limit (elastic modulus value around 250 MPa for compliant matrix and 22 GPa for stiff matrix) regardless of indent location for large contact widths $(2a > 2r)$.

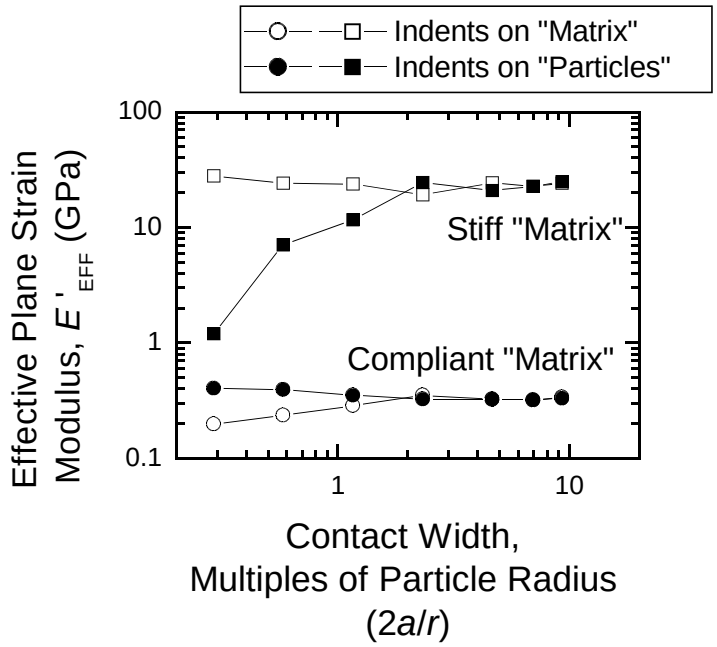

Figure 6-9: Effective elastic modulus (E_{EFF}) as a function of normalized contact width ($2a/r$) from indentation FEA models for composite materials with 50% mineral volume fraction (V_f) and a particle radius of r.

Closer inspection of the stiff phase continuous models demonstrated some small periodic fluctuations in effective elastic modulus at relatively large contact widths. The period of fluctuation was approximately comparable to the interparticle spacing (Figure 6-10) and the magnitude of the variation was around 10%. It is suspected that the periodic response is due to the large stress fields at the indenter corners such that the corners vary in location relative to particle or matrix, creating this periodic response.

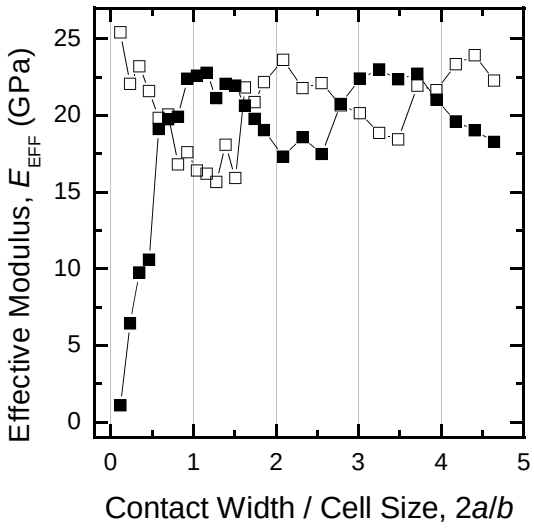

Figure 6-10: Effective elastic modulus (E_{EFF}) for different indent locations (centered on matrix on particles) as a function of normalized contact width (2*a*/*b*) from indentation FEA models for composite materials with 50% mineral volume fraction (V_f) and a unit cell size of *b*.

6.2.3 Indentation Model Applied to Bone and Dentin

The model results presented in Figure 6-9 were compared to the experimental data for bone indentation variability (Figure 3-19). The bone data were plotted on a new *x*-axis scale representing the indentation elastic displacement, h_E, as calculated by

$$h_E = \left(\frac{P_{max}}{\alpha_2 E'} \right)^{1/2} \qquad [6\text{-}8]$$

The experimental plane strain modulus data were converted to elastic modulus assuming $\nu = 0.3$. The *x*-scale in Figure 6-9, the non-dimensional contact width to particle radius ratio (2*a*/*r*) were converted back to elastic indentation displacement by multiplying by *r*/5.6, where *r* was varied until the model and experimental data for the smallest

indentation load levels (P_{max} = 0.1 mN) were aligned. This radius (*r*) was recorded as the critical feature size. The result is shown for bone in Figure 6-11, where the critical feature size was found to be 600 nm.

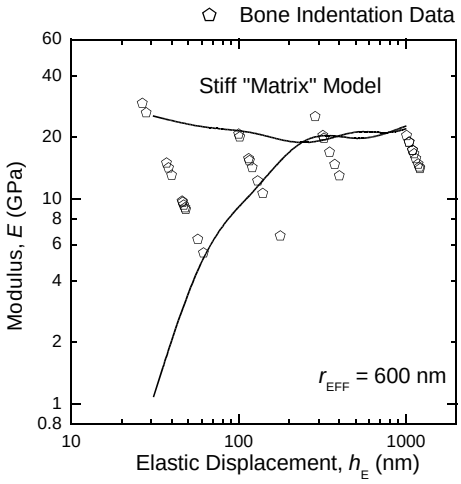

Figure 6-11: Comparison of experimental bone indentation elastic modulus (*E*) as a function of elastic displacement (h_E) with the composite indentation finite element model. The comparison allows for estimation of the smallest critical feature size *r* causing variability in the data, in this case found to be 600 nm.

A similar protocol was followed for the dentin data from Figure 3-20. However, the finite element indentation model had to be re-run with a slightly larger volume fraction of mineral (e.g. smaller interparticle spacing) to account for the on-average larger continuum-level elastic modulus for dentin compared to bone. The particle spacing was varied until the model results matched the experimental data, found to be for an interparticle spacing of 2.9 corresponding to an approximate mineral volume fraction of 0.63. The model results are shown along with the dentin experimental data in Figure 6-12, in which the critical feature size was found to be 100 nm.

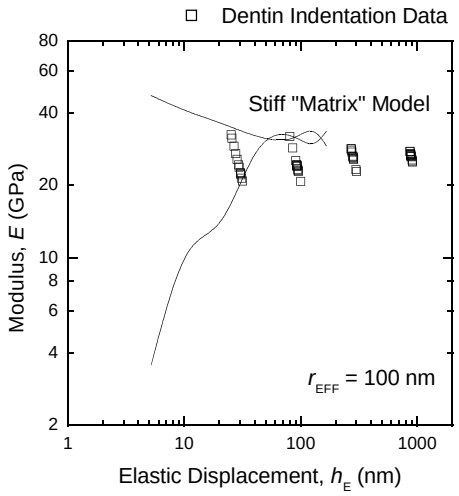

Figure 6-12: Comparison of experimental dentin indentation modulus (E) as a function of elastic displacement (h_E) with the composite indentation finite element model. The smallest critical feature size r causing variability in the data was found to be 100 nm.

The comparison of model and experiment for bone and dentin gives a critical feature size for dentin a factor of six smaller than that for bone. The dentin value may well be closely related to the intrinsic variability of the instrumentation used to make the measurements, since the coefficient of variation for the dentin data did not vary much from that for fused silica (section 3.3).

The critical feature size for bone was found to be 600 nm, which is larger than the size of a single mineral particle but dramatically smaller than the size of large, well-understood structural features of the bone such as osteons. At small indentation loads, such as the 6 mN used in the original study, this length-scale is comparable to the peak indentation depth. Even at large indentation loads, such as 100 mN, the length-scale of the bone features is only about a factor of five smaller than the indentation depth, which helps to explain the persistent variability at these larger indentation loads. The potential for this variability to be due purely to local compositional variations in bone will be examined next.

6.3 Examination of Bone Indentation Variability

In the following section, I will re-examine the question of sources of variability in indentation responses of bone. In doing this, I will use some experimental data collected at Queen Mary, University of London and provided by my frequent collaborators in the Andy Bushby group (this raw data was previously published in the Journal of Anatomy, [Ferguson et al, 2003]). The key element in this data set is the addition of composition information to indentation modulus measurements. The local mineral density (in gm/cm^3) was measured by quantitative back-scattered electron (qBSE) imaging in the location of every indentation test. This additional information, which is not available for the indentation testing performed by myself and reported elsewhere in this work, will allow for examination of these mechanical data within a composite materials framework based on mineral volume fraction. The modeling results from chapter 5 will then be used to interpret this data in terms of mineral phase connectivity.

6.3.1 Background

The original experiments were undertaken on both articular calcified cartilage and underlying subchondral bone from human femoral heads and details can be found in Ferguson et al [2003]. Only the bone data will be examined in this section. Indentation tests were performed and elastic modulus values were obtained. The mineral content at each indentation location was obtained using quantitative back-scattered electron imaging in a scanning electron microscope. Standards were used to establish the quantitative scale for mineral density. Data were provided to me as shown in Figure 6-13, where indentation modulus is plotted against a mineralization number from 0 to 300. The value of 0 corresponds to a mineral density of 1.7 g/cm^3 and 255 corresponds to 2.2 g/cm^3; these values were used with linear interpolation to obtain a value of mineral density for each indent location:

$\rho_c = 1.7 + 0.5^*$ qBSE/255. [6-9]

where "qBSE" is the number value from Figure 6-13.

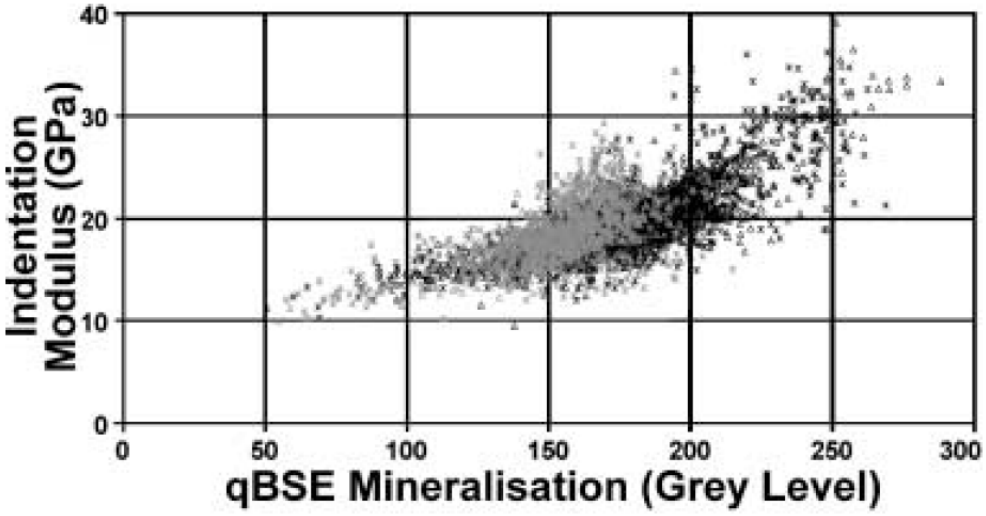

Figure 6-13: Indentation modulus versus qBSE mineralization grey level for subchondral bone (grey points) and articular calcified cartilage (black points) from [Ferguson et al, 2003]

6.3.2 Conversion to Composite Materials Framework

Computed values of the mineral density (ρ_c) from Eqn 6-9 were next converted to approximate volume fractions of mineral assuming an organic phase density of (ρ_o) 1 g/cm^3, an inorganic phase density (ρ_i) of 3.22 g/cm^3 and a rule-of-mixtures assumption:

$$\rho_c = \rho_o (1-V_f) + \rho_i V_f \quad [6\text{-}10]$$

where V_f is the volume fraction of the mineral phase and ($1-V_f$) is the volume fraction of organic phase.

Rearranging Eqn. 6-10 for the inorganic phase volume fraction gives

$$V_f = (\rho_c - \rho_o)/(\rho_i - \rho_o) \qquad [6\text{-}11]$$

The minimum, maximum, and mean values of both volume fraction mineral and modulus for the bone data shown in Figure 6-13 (2079 individual data points) are shown in Table 6-1.

Table 6-1: Mean and ranges of mineral volume fraction and elastic modulus seen in the subchondral bone indentation data [Ferguson et al, 2003]

	Minimum	***Mean***	***Maximum***
Mineral fraction, V_f	0.36	0.45	0.51
Modulus, E (GPa)	9.97	18.36	29.2

The data for elastic modulus was plotted as a function of mineral (inorganic) volume fraction and compared with the Hashin-Shtrikman composite bounds. Resin-embedded mineralized tissue samples were considered as a two phase organic-inorganic composite. The mineral phase was assumed to have an elastic modulus (E) of 100 GPa and Poisson's ratio of 0.3. The organic phase was considered as a hybrid of collagen (E ~ 100 MPa) and poly (methyl methacrylate) embedding resin (E ~ 5 GPa) with an elastic modulus of 2.5 GPa and a Poisson's ratio of 0.35 [Ferguson et al, 2005]. The plot of bone modulus versus mineral volume fraction is shown in Figure 6-14. It is apparent immediately that simply accounting for the local mineral volume fraction is not sufficient to account for the variability in indentation modulus values seen in Figure 6-14. The data lie clearly between the Hashin-Shtrikman bounds for modulus. The overall trend in E with V_f has two regions: (1) at smaller mineral volume fractions (< 0.45) the modulus increases gradually with V_f, (2) at larger mineral volume fractions (>0.45) the modulus ranges widely, with some values approaching the upper H-S modulus bound.

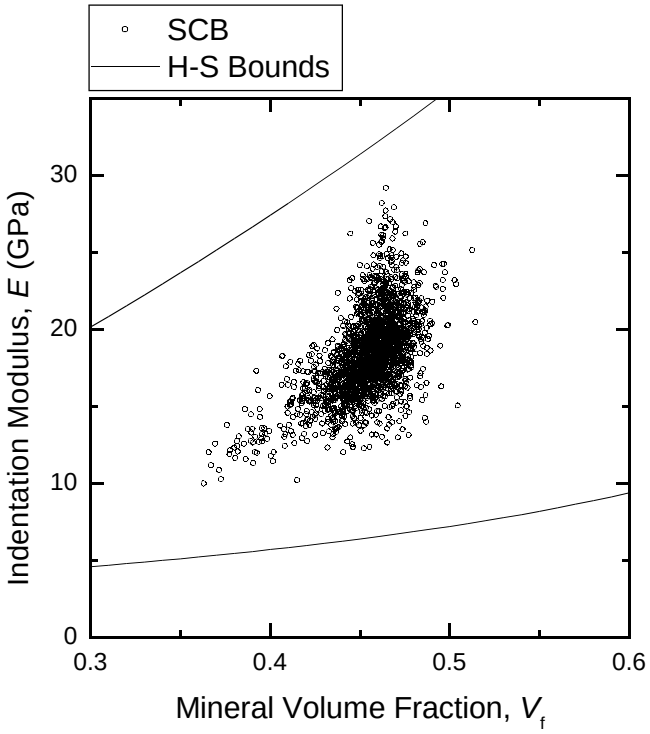

Figure 6-14: Indentation elastic modulus (E) versus mineral volume fraction (V_f) for subchondral bone. Raw data from [Ferguson et al, 2003] (Figure 6-13) converted from qBSE number to mineral volume fraction using Eqn. 6-11 for the current work.

For further quantitative analysis of this data, the values for volume fraction were rounded to two significant figures, and averages and standard deviations of the elastic modulus were calculated for each volume fraction. These data are plotted in Figure 6-15 along with the best fit line, which has the equation:

$$E \text{ (GPa)} = 80\ V_f - 18 \qquad [6\text{-}12a]$$

This is approximately the same as the best fit line for the raw data (Figure 6-14), which has the best-fit line:

E (GPa) = 83 V_f – 19 [6-12b]

The average modulus is thus well-predicted by a direct relationship with mineral volume fraction over this range of volume fraction values.

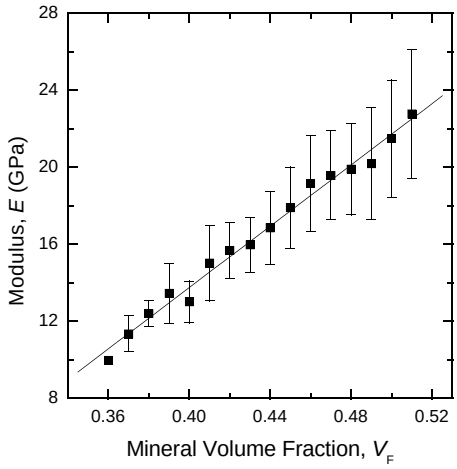

Figure 6-15: Modulus (E) data averaged for mineral volume fraction (V_f) data binned in rounded increments of 0.01 and line-fit.

Consistent with the broadening in data seen in Figure 6-13, although there are many more observations at larger mineral volume fractions (especially in the range 0.43-0.48) the standard deviation is larger.

When the mean modulus is examined as a function of volume fraction, within the context of the Hashin-Shtrikman bounds (Figure 6-16), it is seen that the set of averaged bone data lie well between the bounds but are approximately parallel to the upper bound. Based on the examination presented in Chapter 5 (Figure 5-27), this indicates that *on average* the modulus changes with mineral fraction are due to composition changes and not due to changes in the overall mineral network structure or connectivity (Figure 5-29).

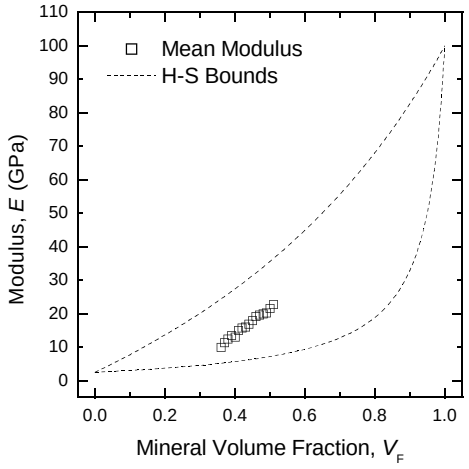

Figure 6-16: Average modulus (*E*) data for volume fraction (V_f) binned in increments of 0.01 (rounded) . Data are presented in context of the Hashin-Shtrikman bounds for a composite of mineral (*E* = 100 GPa) and hybrid collagen/PMMA (*E* = 2.5 GPa)

To examine the distribution of modulus values, and variations not due to mineral volume fraction, modulus data for fixed volume fraction values near the mode value (0.46) are plotted as a series of histograms in Figure 6-17. There is dramatic variation in modulus at fixed mineral volume fraction. The distributions are in general not symmetric, with more values present at larger modulus values and therefore a greater distance between the mean and maximum than the mean and minimum. At larger mineral volume fractions, the minimum modulus value does not change much but the maximum value increases with mineral fraction.

These data all agree well with the observations of Katz [1971] that modulus values for bone cannot be predicted by only mineral volume fraction. Clearly local geometry and structure is critically important in determining bone modulus. The implication for the bone modulus maps presented in Chapter 3 is also clear—there is more to this dramatic point-to-point property variation in bone than just local composition. The data from Figure 6-14 will next be considered within the context of the finite element modeling results presented in chapter 5.

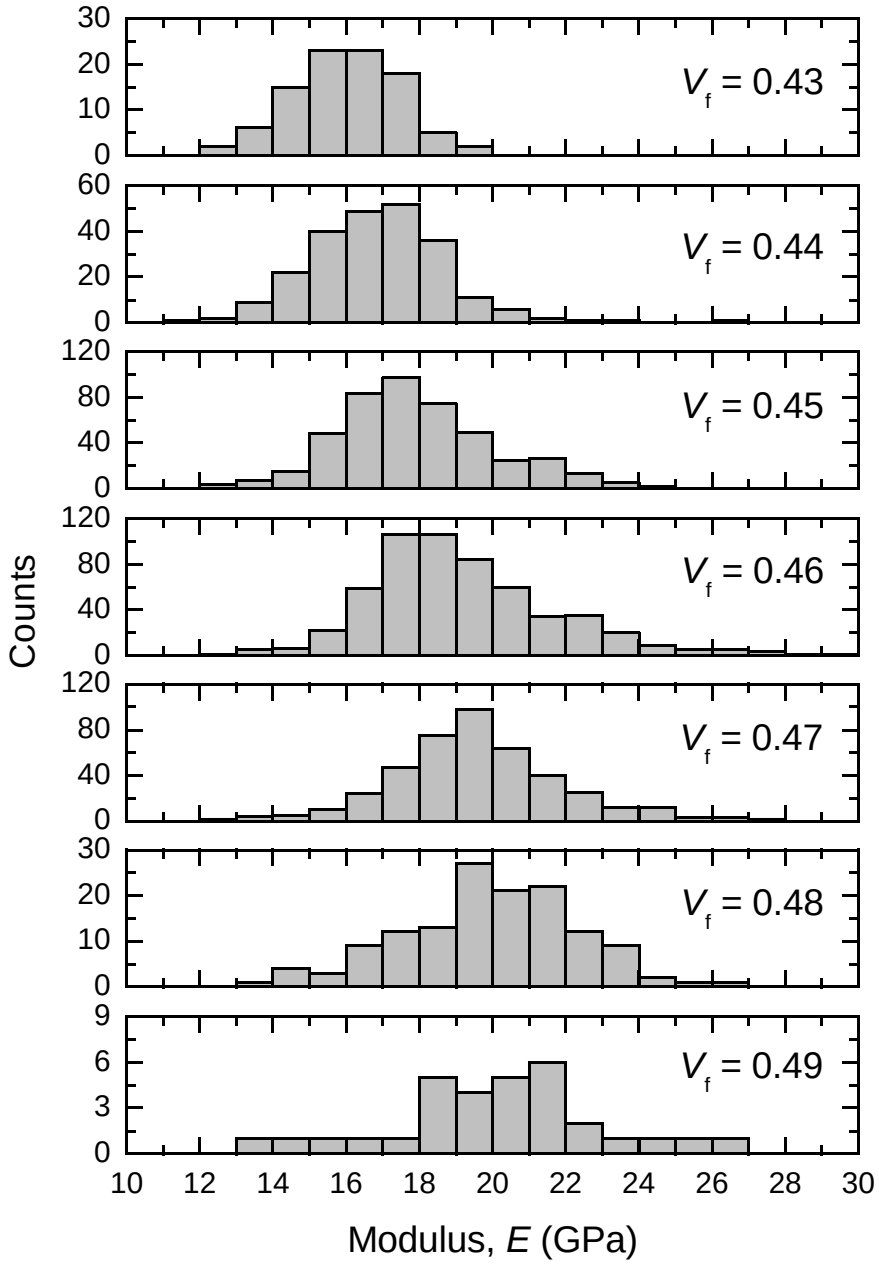

Figure 6-17: Histograms of observed elastic modulus (*E*) values for mineral volume fraction levels from 0.43 to 0.49. The mean and maximum values increase with volume fraction while the minimum remains approximately fixed at about 12 GPa.

6.3.3 Estimates of Bone Structure from Modulus

The elastic modulus data can be used to estimate the connectivity based on the results in Chapter 5. The mean and range for connectivity fraction (F^{cxn}) at each volume fraction (V_f) was calculated from the mean, minimum, and maximum values of the experimental elastic modulus (E) relative to the Hashin-Shtrikman upper bound $\left(E^{U}_{H-S}\right)$:

$$F^{cxn} = \frac{E}{E^{U}_{H-S}} \qquad [6\text{-}13]$$

The mean (horizontal bars) and range (vertical bars) for the estimated connectivity fraction (F^{cxn}) are shown in Figure 6-18 for the experimental data presented above (Figure 6-14). Several features of this plot are striking. Because the minimum modulus value was reasonably constant, the minimum connectivity appears to be fixed at approximately 0.40. At intermediate values of the volume fraction, the maximum calculated connectivity is quite high, around 0.8-0.9, such that the apparent range of connectivity values at fixed volume fraction is large, about 0.5. The mean presumed connectivity increases linearly from approximately 0.4 to 0.6 over the range of volume fractions shown (0.36 to 0.51).

The estimate of connectivity using the current approach is dependent on the Hashin-Shtrikman bounds, which are in turn dependent on the component modulus values chosen to generate the bounds. For the finite element models, the component phase modulus values are well known. For mineralized tissues, as was discussed extensively in Chapter 5, the component phase values are not very well known, especially in biologically derived structures (*e.g.* hydroxyapatite mineral plates in bone compared to laboratory-derived or naturally occurring apatite). As was shown in Chapter 5, for $E_{mineral} >> E_{collagen}$, the upper bound is reasonably independent of the collagen modulus. However, the connectivity estimates depend heavily on the mineral modulus assumed, which was assumed to be 100 GPa here. All calculated connectivity

fractions would shift with a change in the mineral modulus. As such, an independent measurement of the structural connectivity is necessary to achieve quantitative numerical connectivity values for mineralized tissues. The relative values, however, and trends with volume fraction can be examined in some confidence. It seems that advances in microscopy and other advanced technologies will be required before the ultrastructure of bone and allied tissues can be examined at the length-scales discussed here, sub-nm to nanometer, since the sample preparation techniques associated with traditional electron microscopy analysis have been implicated as changing the connectivity of the mineral network [Benezra-Rosen et al, 2002].

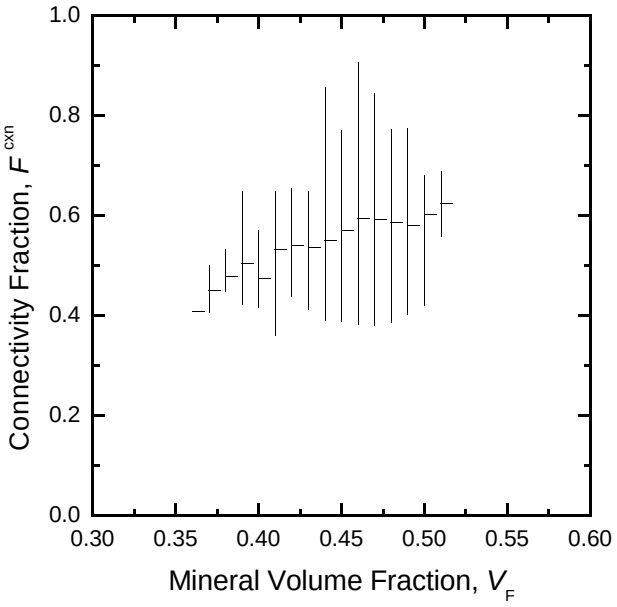

Figure 6-18: Mean (horizontal bars) and range (vertical bars) of calculated connectivity fraction *F* for subchondral bone data shown in Figs 6-13 and 6-14.

6.4 Embedded Bone

In this section, an attempt is made at directly characterizing the connected fraction of mineral in bone, and to do so as a function of orientation. To do this, experimental modulus-mineral content (E-V_f) data was again provided via my recent collaborations with the Bushby group at Queen Mary, University of London . Bone samples were examined as two- or three-phase composite structures as follows [Bushby et al, 2004 ; Bembey et al, 2005]: (1) dehydrated mineral-protein composite but with poly (methyl methacrylate, PMMA) resin filling the voids resulting in three solid phases, (2) as a PMMA-mineral composite following protein removal and replacement with PMMA, and (3) as a PMMA-protein composite following mineral removal and replacement with PMMA. The following section contains a novel composite materials analysis of these samples.

6.4.1 Background

At the ultrastructural level, bone can be thought of as a three phase co-continuous composite consisting of collagen and other proteins, bone mineral and water. When the bone is dehydrated and embedded with PMMA resin, the resin fills the original water space and results in a fully-dense three-phase composite of collagen, mineral, and PMMA.

In this section the bone samples utilized were cortical bone from mid-shaft of the equine third metacarpal. Mid-shaft dorsal cortical tissue from the equine third metacarpal bone is relatively dense and uniform with low porosity. Measurements were made in directions parallel and normal to the long axis of the tissue to establish anisotropy effects.

Cortical bone specimens were machined from the metacarpal bone from two-year old thoroughbred horses. Rectangular bone beams (~5×2×25mm), stored frozen prior to machining, were excised from the mid-shaft of the dorsal cortex. Rectangular beams

were prepared for nanoindentation in the following categories:

1. dehydrated in 100% ethanol and subsequently **embedded** in (PMMA). The ethanol was replaced with acetone, the acetone with MMA monomer, and polymerized at 37°C and then cured at 50°C.
2. **deproteinated** in Sodium Hypochlorite, and embedded in PMMA.
3. **decalcified** in HCl, and embedded in PMMA.

Mechanical testing and data analysis were reported previously for these samples [Bushby et al, 2004 ; Bembey et al, 2005] and the results are summarized in Table 6-2. The mineral concentration was measured for the embedded samples using the same technique as was described in section 6.3.

Table 6-2: Indentation moduli (E_i) and anisotropy ratio for bone in different conditions (1-direction = longitudinal; 2-direction = transverse)

Condition	E_1 (GPa)	E_2 (GPa)	E_1/E_2
(1)Embedded	22.9	17.7	1.29
(2)Deproteinated	17.4	10.9	1.6
(3)Decalcified	4.6	4.3	1.07

6.4.2 Analysis

The effect of anisotropy in Berkovich indentation measurements of bone is well established [Swadener et al, 2001]. Based on integration of measured bone elastic constants over the indented plane, it can be shown that an anisotropy elastic modulus ratio of 1.75 (e.g. ratio of longitudinal to transverse moduli) corresponds to an indentation modulus anisotropy ratio of approximately 1.4 [Swadener et al, 2001]. Following the integration, the minimum indentation modulus (*e.g.* transverse) is greater than the minimum elastic modulus, and the maximum indentation modulus (*e.g.* longitudinal) is less than the maximum elastic modulus. The indentation anisotropy ratio (E_1/E_2) of 1.3 seen in the current study is in good approximate agreement with the value of 1.4 seen by Swadener et al [2001].

The elastic modulus anisotropy ratio of around 1.75 corresponds to a particle aspect ratio of 1.2 to 2.5 based on finite element modeling (Figure 6-19). This value is far less than the physical aspect ratio seen for individual bone mineral crystals [Currey, 2001] and implies that, in contrary to some recent ultrastructural models of bone [Jager and Fratzl, 2000; Kotha and Guzelsu, 2002; Gao et al, 2003], the anisotropic mechanical response of bone is ***not*** being controlled by individual mineral crystals.

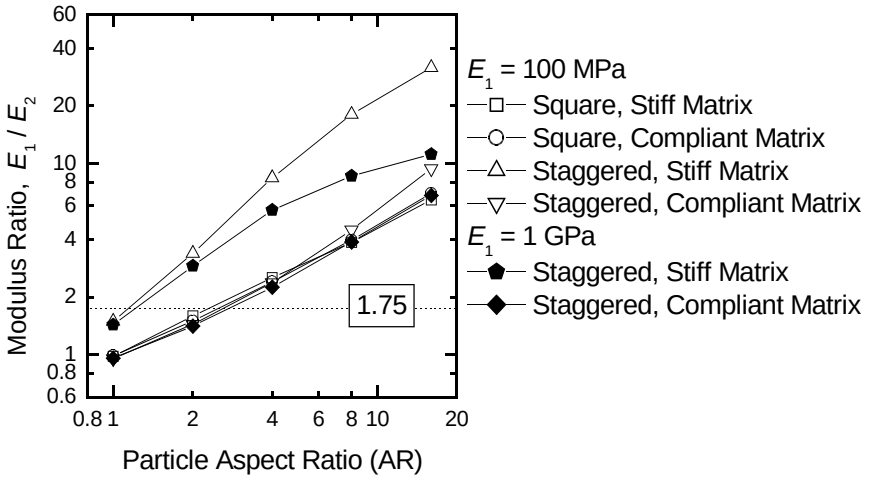

Figure 6-19: Anisotropy modulus ratio (E_1/E_2) for plane strain finite element models of a bone-like material with rectangular particles of aspect ratio (AR) 1 to 16 (reproduced from Figure 5-8). The measured anisotropy ratio for bone is at maximum about 1.75 [Swadener et al, 2001], which corresponds to "particle" aspect ratios of 1.2 to 2.5, depending on the particle arrangement.

An analysis of the composite composition and structure of bone can be undertaken by examination of the different configurations. This analysis will be done independently for the longitudinal and transverse orientations. A working hypothesis for this analysis is that the mineral in bone is split between two physical configurations, one a fully-connected mineral network and the other as disconnected mineral present in and associated with the organic phase. Although there is a slight difference between indentation modulus values and elastic modulus values obtained from tensile tests [Swadener et al, 2001], the experimentally-obtained indentation values are used directly

in the following analysis to approximate elastic modulus values.

First a calculation is done for the connected mineral phase volume fraction, utilizing the the PMMA-mineral composite following protein removal (condition (3) above). The bone sample remains physically intact following deproteination, implying that the remaining material is connected mineral (Figure 6-20a). This assumption was used to calculate the connected mineral volume fraction from the H-S composite bounds.

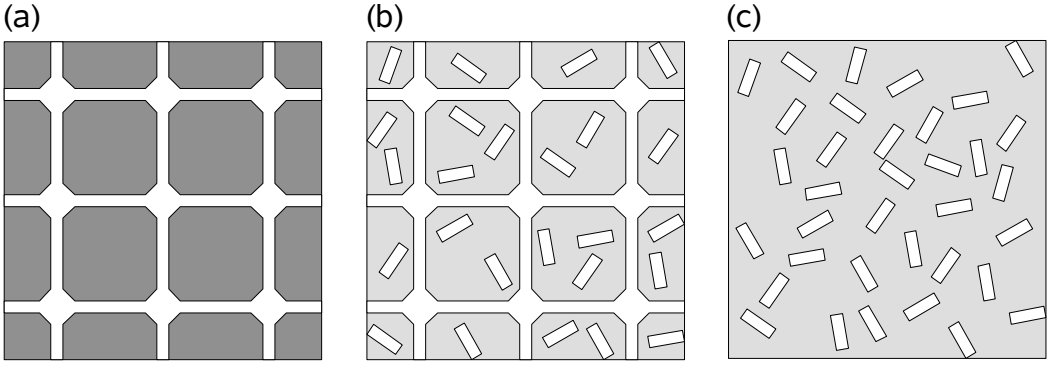

Figure 6-20: Structures representing a composite with both connected and disconnected mineral (mineral shown as white): (a) fully connected mineral phase; (b) composite structure with both connected and disconnected mineral; (c) fully discrete and disconnected mineral phase.

The experimental (indentation-based) value of the modulus for the deproteinated bone sample (17.4 GPa, longitudinal; 10.9 GPa, transverse; Table 6-2) is shown in Figure 6-20 along with the Hashin-Shtrikman composite bounds for a PMMA-mineral composite. The PMMA modulus is well known (4 GPa) [Bushby et al, 2004] and the apatite is assumed to be fully dense with a modulus of 150 GPa (from indentation tests of pure apatite, section 3.3.1 above). The modulus value for a connected mineral network is associated with the upper Hashin-Shtrikman bound, as shown in Figure 6-21, and gives a mineral concentration of 16% by volume for the longitudinal measurement and 9% for the transverse measurement.

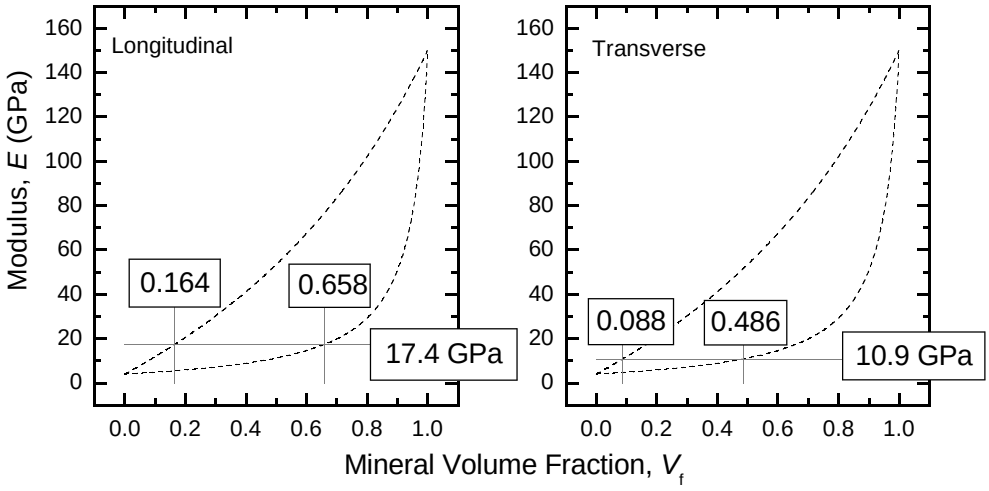

Figure 6-21: Hashin-Shtrikman modulus bounds for a composite of PMMA resin (*E* ~ 4 GPa) and apatite (*E* ~ 150 GPa). The measured longitudinal modulus (17.4 GPa) corresponds to a mineral volume fraction of 0.16 for mineral as a fully-connected phase; the measured transverse modulus (10.9 GPa) corresponds to a mineral volume fraction of 0.09 for mineral as a fully-connected phase.

The connected mineral volumes are clearly too small to be representative of the total mineral content of bone samples. The remaining mineral was assumed to be disconnected from the mineral network structure (Figure 6-20c), by virtue of being associated with the collagen that was removed during deproteination. The effect of disconnected mineral (in the organic phase) was examined by consideration of the fully dense mineral-collagen-resin structures (*e.g.* native bone with resin infiltration due to embedding) and considering the structure as the composite structure shown in Figure 6-20b with both the connected mineral, as calculated above, and also some disconnected mineral. Disconnected mineral would affect the "matrix" modulus (e.g. raise the collagen-PMMA composite modulus by virtue of the collagen mineralization; since the decalcified samples showed modulus values comparable to pure PMMA, the collagen-PMMA phase was assumed to be uniformly comparable to the PMMA phase with modulus of 4 GPa) and so by raising the compliant phase modulus from 4 GPa to some

greater value. For the longitudinal direction, this "matrix" modulus would have to be 9.6 GPa to raise the overall bone sample modulus value to 22.9 GPa at fixed connected mineral volume fraction of 0.164. For the transverse direction, the "matrix" modulus required to obtain the full-embedded modulus value of 17.7 GPa at fixed connected mineral fraction of 0.088, the matrix modulus would have to be 10.8 GPa.

The values of "matrix" (collagen-PMMA-isolated mineral) modulus can be deconvoluted to obtain a disconnected mineral volume fraction by considering this matrix as the structure in Figure 6-20c, and thus by using the lower H-S bound for a mineral-PMMA composite. The longitudinal value of 9.6 GPa corresponds to a "matrix" phase with disconnected mineral fraction of 43%. The transverse value of 10.8 GPa corresponds to a "matrix" phase with disconnected mineral at 48% by volume.

From the two independent populations of mineral, connected and disconnected, the total mineral volume fraction in the composite can be calculated. For the longitudinal direction, where 16% of the volume is occupied by connected mineral, the "matrix" phase occupies 84% of the volume and has 43% mineral. This gives an additional 36% mineral volume fraction of the total structure, which can be combined with the 16% connected mineral to give a total mineral fraction estimate of 52%. Similarly, for the transverse direction 9% of the total volume is occupied by connected mineral, and the mineral contained in the matrix phase adds 44% to the volume of the total structure, giving a total mineral fraction of 53% in the sample. These calculated values of the mineral content of bone samples (52-53%) obtained indirectly by purely mechanical considerations, and calculated independently in each direction, are found to be in excellent agreement with the sample mineral content measured by quantitative back-scattered electron imaging (qBSE) the value for which was found to be 49.5%.

The approach here offers a new hypothesis for the observed anisotropy of bone. The calculated disconnected mineral concentration in the longitudinal and transverse directions was approximately the same, 43% or 48%, while the connected mineral concentration was different by approximately a factor of two, 16% longitudinally versus 9% transversely. The anisotropy in bone modulus values can therefor be explained to a

first approximation by differences in the relative proportion of isolated and connected mineral—the mineral is approximately one third (0.31) connected in the longitudinal direction and only about one fifth (0.17) connected in the transverse direction, by the calculations performed in the current work. Further structural-mechanical analysis of bone is needed to compare to the current investigation, but the ideas presented here—for a two-part separation of the mineral in bone, as well as for structural anisotropy resulting from phase connectivities that vary with direction—are promising ideas that warrant further examination.

The connectivity fraction (F^{cxn}) estimation technique, based on elastic modulus, as discussed in sections 5.6 and 6.3.3 can be compared with the results here. The modulus values for longitudinal (22.9) and transverse (17.7) directions can be compared to a value for 50% mineral (53.5) to calculate a connectivity fraction (F^{cxn}) using equation 5-15, which gives 0.28 for longitudinal and 0.15 for transverse. These are excellent estimates of the values seen above (based on direct calculations) of 0.31 for longitudinal and 0.17 for transverse.

6.5 Discussion

In nanoindentation experiments, especially at small depths, the volume displaced by the indenter is small enough to allow for individual tip-mineral platelet interactions. Therefore indentation at small length scales is going to give a discrete measurement of local structure, not a continuum-level mechanical property measurement. It was found here that the length-scales associated with bone variability were large, more than half of a micrometer, while for dentin they were quite small, around 100 nm. This size difference is relevant in standard operational indentation testing: for indentation tests conducted at 100 mN, the typical value used in much of the experimental work in the current study including the property mapping study (section 3.4), the indentation depths were 2-4 μm for bone and about 2.5 μm for dentin. The dentin indentation tests (at 100 mN) were conducted at depths more than an order of magnitude more than the variation length-scale, while the bone tests were at only a few times this length-scale at this same indentation load. Therefore the fact that these two tissues showed such different patterns of indentation variability in the property mapping experiment becomes more understandable, and a recommendation can be made for bone properties to be examined at even larger indentation loads than were used here in the experimental Chapters 3 and 4. However, larger loads (and length-scales) takes the measurements out of the range of commercial nanoindentation machines.

A question arises as to how much of the variability seen in indentation data can be explained by the variations in local mineral volume fraction. From the linear fit to the raw data (Eqn. 6-12b) the correlation coefficient $R = 0.57$, which gives $R^2 = 0.32$. Thus only 32% of the total variation in the data can be attributed to variations in volume fraction using a simple linear modulus-volume fraction model (a good approximation for the upper modulus bound). It seems that the minimum modulus (Table 6-1) is well-predicted from the minimum volume fraction by Eqn. 6-12 but, the maximum observed modulus is much higher than the prediction from the maximum mineral volume fraction, and this is consistent with the extremely large modulus (or connectivity) values observed

at intermediate mineral volume fraction levels. It is also clear from the fact that the minimum modulus is approximately fixed with volume fraction, and from observations of the increasing standard deviation with mineral volume fraction in Figure 6-15, that the variability in bone modulus appears to become greater with larger mineral volume fractions.

Roughly two-thirds (68%) of the variability in bone elastic modulus is due to factors other than the local mineral volume fraction, namely geometrical factors such as the local structure, orientation and arrangement of mineral, while one third is directly attributable to the local mineral concentration. An interesting observation is that the variability in responses appears to rise with mineral volume fraction, which for the bone data in Section 6.3 ranges from 0.36 to 0.51. There is an interesting thermodynamic analogy that may be relevant in this circumstance, that of configurational entropy and mixing of solutions. As the composition of a two-component solution approaches a 50%-50% mixture, the number of possible configurations or arrangements of the two components increases, and in fact reaches a maximum at a half-and-half mixture. Therefore, a material such as bone with a roughly 50-50 blend of organic and inorganic materials would in fact be expected to have a large potential range of arrangements of the phases, leading in turn to large elastic modulus variations. Within this context, it becomes reasonable to expect that enamel, with a limited non-mineral phase fraction would indeed be reasonably uniform in response, because there is not a great deal of potential variation in the arrangements of the components. The then-puzzling question that arises is as to the perceived lack of variability in the dentin response, which also hovers at a near 50-50 blend of organic and inorganic phases. The length-scale issue becomes relevant here, in that the apparent length-scale for dentin was so much smaller than that for bone, and perhaps we are just not able to sense the local variability in dentin with the tools used in the current investigation. Another feasible hypothesis is that for some reason there is a reasonably regular arrangement of phases in dentin, due to some thermodynamically stable configuration that does not exist in bone.

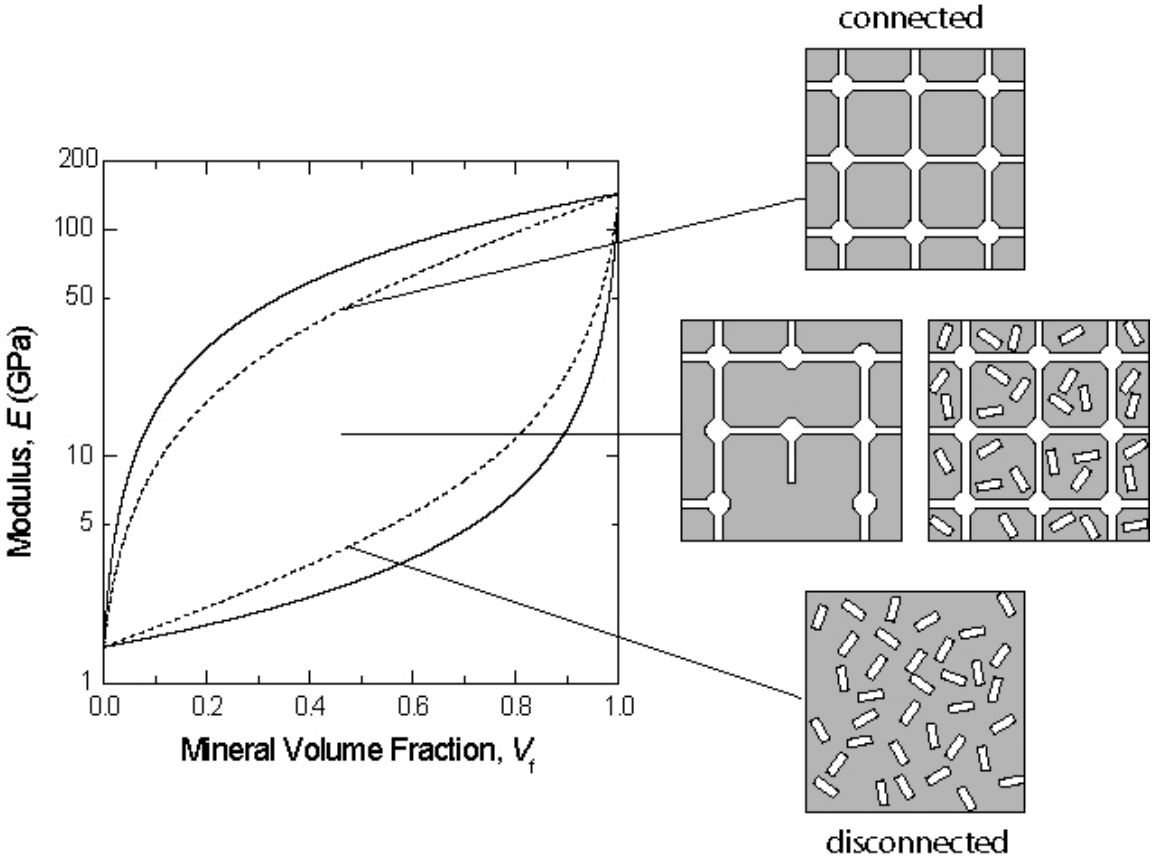

Figure 6-22: Illustration of the relationship of structures with different mineral phase connectivity to the Hashin-Shtrikman modulus bounds.

A summary of much of the work contained in the last two chapters of this work is provided in Figure 6-22. Two different "partially connected" structures are shown for the modulus values that occur between the bounds (middle figures), one a connected structure with missing "links" (section 5.6) and the other a mixture of free and connected mineral (section 6.4). Either of these structures could be found in mineralized tissues, and more structural examination of the mineral network will be required to definitively establish which structure is more physically realistic.